



PCCP

**Pressure-Induced Metallicity and Piezoreductive Transition  
of Metal-Centres in Conductive 2-Dimensional Metal-Organic  
Frameworks**

Journal:	<i>Physical Chemistry Chemical Physics</i>
Manuscript ID	CP-ART-08-2019-004797.R2
Article Type:	Paper
Date Submitted by the Author:	01-Nov-2019
Complete List of Authors:	Le, Khoa; University of Oregon, Chemistry and Biochemistry Hendon, Christopher; University of Oregon

SCHOLARONE™  
Manuscripts

## Pressure-Induced Metallicity and Piezoreductive Transition of Metal-Centres in Conductive 2-Dimensional Metal-Organic Frameworks

Received 00th January 20xx,  
Accepted 00th January 20xx

DOI:

Khoa N. Le and Christopher H. Hendon\*

Due to their generally poor conductivity, metal-organic frameworks (MOFs) have been limited in electrical applications. The highest performing materials are two-dimensionally connected  $\text{Ni}_3(\text{hexaiminotriphenylene})_2$  and  $\text{Ni}_3(\text{hexaiminobenzene})_2$ ; both feature experimental conductivities exceeding 500 S/m. From theory, both are predicted to be bulk metals but the former is known to be a semiconductor within a single monolayer. In this work we explore structural deformation as a route to augmenting the electronic properties of these two high performing materials. We show that, under hydrostatic negative pressure, metallicity can be installed in the  $\text{Ni}_3(\text{hexaiminotriphenylene})_2$  monolayer. Further, we predict a unique piezoreduction of metal ions and induced-magnetization in  $\text{Ni}_3(\text{hexaiminobenzene})_2$  due to the shift in energy of metal-ligand bonding and antibonding orbitals. These observations aid in our understanding of how MOFs conduct electricity and may also be used as a design principle in future MOF technologies.

### Introduction

Previous studies of MOFs have shown that this class of structurally diverse materials are unique due to their porous architecture and resultant high surface areas.<sup>1–3</sup> The application of a particular MOF depends on the chemistry of both the inorganic metal ions/clusters and the organic linkers. Considering their structure and composition, MOFs have been decidedly useful in gas separation and storage,<sup>4–7</sup> catalysis,<sup>8</sup> drug delivery,<sup>9,10</sup> and energy-related applications such as light harvesting,<sup>11</sup> thermoelectrics,<sup>12</sup> and supercapacitors.<sup>13,14</sup> In case of the latter, a MOF's utility is intimately related to its electrical conductivity. Thus improving electronic delocalization is paramount if these scaffolds will be useful in energy storage devices.<sup>15–18</sup>

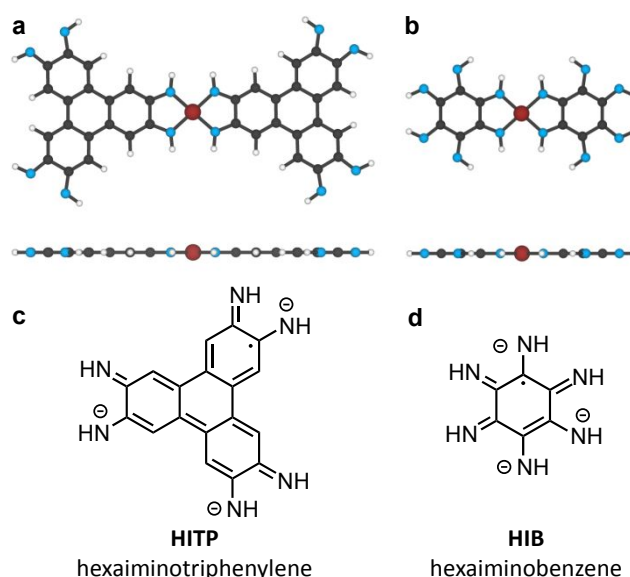


**Figure 1.** A portion of **a)**  $\text{Ni}_3(\text{HITP})_2$  and **b)**  $\text{Ni}_3(\text{HIB})_2$ . The oxidation state and one resonance depiction of each ligand is presented in **c** and **d**, respectively. Atoms are depicted in C – black, N – blue, H – white, and Ni – magenta.

However, most MOFs are wide gap electrical insulators with heavy charge carrier effective masses<sup>19,20</sup>. These properties stem from their highly ionic metal-ligand interface<sup>21</sup>. Furthermore, the only successful route to doping a metal-organic framework relies on the redox properties of the ligand and/or metal. This approach has been fruitful; redox-induced charge hopping<sup>22–26</sup> has been shown to result in increased electrical conductivity. But given most charge carriers are formed thermally, the band gap, and nature of the frontier orbitals and their corresponding energetics is of critical importance for generating conductive scaffolds.

Two of the highest performing conductive MOFs,  $\text{Ni}_3(\text{HITP})_2$  (HITP  $\equiv$  2,3,6,7,10,11-hexaminothriphenylene) and  $\text{Ni}_3(\text{HIB})_2$  (HIB  $\equiv$  hexaiminobenzene) are 2D-connected bulk metals (truncated building blocks are shown in Figure 1), with corresponding electrical conductivities of  $\sim 60$  S/cm<sup>27,28</sup> and  $\sim 80$  S/cm<sup>29</sup>, respectively. Despite their structural similarities,

<sup>a</sup> Department of Chemistry and Biochemistry, University of Oregon, Eugene, OR, 97403, USA.

\* To whom correspondence should be addressed:  
Twitter: @chendon

Email: chendon@uoregon.edu

Electronic Supplementary Information (ESI) available: Geometric structures used in DFT calculations. See DOI: 10.1039/x0xx00000x

monolayer  $\text{Ni}_3(\text{HITP})_2$  features a discrete  $\sim 0.2$  eV band gap;<sup>30</sup> electrons are thought to conduct in the bulk material in the non-covalent  $\pi$ -stacked direction, perpendicular to the covalent sheets.<sup>31</sup> Foster and colleagues further explored this by demonstrating that  $\text{Ni}_3(\text{HITP})_2$  undergoes a metal-to-semiconductor transition by separating its sheets (either through chemical pillaring or otherwise).<sup>30</sup> Conversely,  $\text{Ni}_3(\text{HIB})_2$  is metallic in-plane but insulating in the bulk non-covalent directions.<sup>29</sup> The electronic dissimilates between these two scaffolds are governed by the electronic differences of the ligand (one resonance structure for each are shown in Figure 1c and 1d). In both syntheses the ligand is required to be triply oxidized and deprotonated six times to yield a charge neutral scaffold.

Ideally, these 2D connected MOFs would feature metallic character in all directions, minimizing the reliance of crystallographic packing in the non-covalent axis. However, without augmenting the composition of the MOF, there are no reports of the installation of a semiconductor-to-metal transition in the  $\text{Ni}_3(\text{HITP})_2$  monolayer. Here we propose the application of pressure to modulate the electronic structure of these conductive scaffolds in order to obtain novel electronic properties from these promising conductive scaffolds.

Hydrostatic pressure, both positive and negative, may be experimentally applied mechanically, or by thermal expansion, gas adsorption,<sup>32,33</sup> etc. In some cases, this process can result in amorphization, phase transitions, and other structural changes of the frameworks,<sup>34–37</sup> but MOFs are known to be stable up to relatively high pressure and temperature.<sup>38–40</sup> With this in mind, the effect of pressure on the electronic structure of both  $\text{Ni}_3(\text{HITP})_2$  and  $\text{Ni}_3(\text{HIB})_2$  has not been previously examined. Here, we demonstrate that under facile lattice expansion,  $\text{Ni}_3(\text{HITP})_2$  becomes an in-plane metal. Further, we observe  $\text{Ni}_3(\text{HIB})_2$  undergoes electronic re-ordering

Models of bulk  $\text{Ni}_3(\text{HITP})_2$  and  $\text{Ni}_3(\text{HIB})_2$  are complicated because the interplane potential energy surface is relatively shallow<sup>25</sup>. However, much can be gained from examination of the monolayer, as a single sheet allows us to monitor the electronic properties within the covalent plane without having to examine the emergences of magnetic ordering or other secondary effects. Following the procedure detailed in the computational methods, we assess the effect of pressure through the lens of the electronic band structure, density of states, and magnetic properties in the monolayer.

Based on prior work<sup>41</sup>, we hypothesized that the addition of pressure would stabilize bonding interactions, while destabilizing their antibonding partners<sup>42</sup>. Further, since the metal-ligand bonds are weaker than the organic covalent bonds of the ligand, geometric alterations to the framework are expected to be most evident at the metal-ligand interface. Thus, we hypothesize that bands that contain Ni-N bond characteristics will display larger energetic shifts than, for example, bands associated with the conjugated carbon backbone.

Lattice contractions are expected to also increase band dispersion in due to increased inter-atomic interactions.<sup>42</sup>  $\text{Ni}_3(\text{HITP})_2$  exhibits a minor increase in band curvature (+0.05 eV, Figure 2a) compared to its equilibrium structure. Similarly,  $\text{Ni}_3(\text{HIB})_2$  is persistently a metal even and at high pressure (43 kB, Figure 3a) metallic bands become marginally more disperse (+0.03 eV).

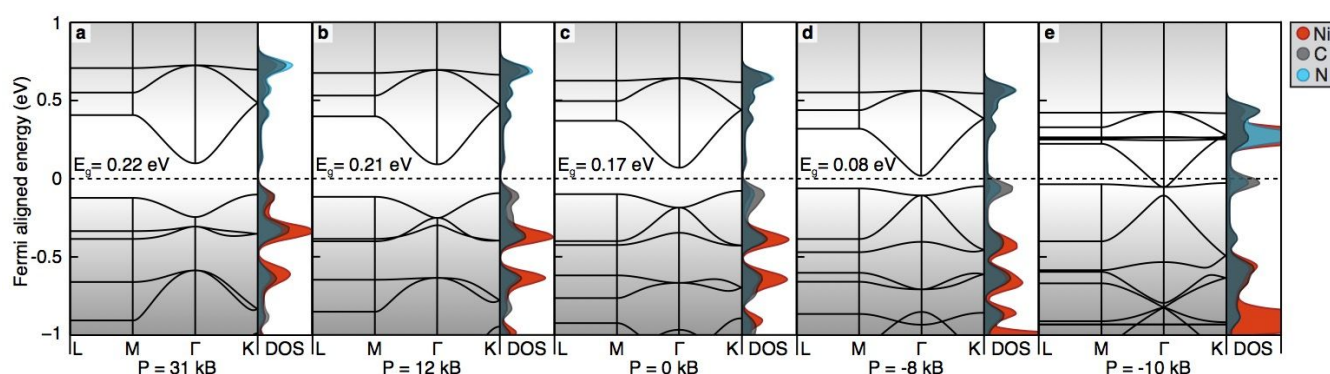


**Figure 2.** Electronic band structures and density of states plots for  $\text{Ni}_3(\text{HITP})_2$  under five representative hydrostatic pressures. Ni-N antibonding bands drop in energy upon lattice expansion, and are evident above the conduction band at -10 kB. The k-path from L-to-M (0.5,0,0.5-to-0.5,0,0) corresponds to the non-covalent direction and are flat because they are sampling perpendicular to the layer. M-to- $\Gamma$ -to-K sample in the intraplane covalent vectors (0.5,0,0-to-0,0,0-to-0.33,0.33,0).  $\text{Ni}_3(\text{HITP})_2$  becomes metallic at low pressure.

to reduce  $\text{Ni}^{2+}$  to  $\text{Ni}^{1.33+}$  while oxidising each ligand by 1  $e^-$ , an effect we term “piezoreduction”.

## Results and Discussion

Conversely, one might expect that a hydrostatic expansion of the frameworks would feature a similar but opposite electronic response to that of a contraction (*i.e.* a band gap/dispersion reduction with lattice expansion). Through the application of negative pressure (*i.e.* stretching the framework) we note that  $\text{Ni}_3(\text{HITP})_2$  features a reduced band gap by 9 meV at -8 kB and, at an applied pressure of approximately -10 kB the material becomes metallic (Figure 2d,e). The metallicity evidently arises from the installation of degeneracy of carbon-based bands at the  $\Gamma$ -point. Importantly, the addition of negative pressure provides a novel route to converting  $\text{Ni}_3(\text{HITP})_2$  into a 2D metal, as evidenced by the non-zero density of states at the Fermi level (Figure 2e). This result has obvious implications for the expected electrical conductivity of the framework, as in-plane conduction would no longer be thermally activated. Additionally, while the metallic transition may not have been experimentally isolated due to difficulties in growing single crystals and measuring their conductivity, we expect that in plane conduction does contribute to the bulk, pressed-pellet measurements. Furthermore, the metallic transition occurs around -10 kB, pressures that should be accessible at high gas loadings or accessible at high temperatures.

The electronic band structure of monolayer  $\text{Ni}_3(\text{HITP})_2$  also reveals the emergence of Ni-N centred bands appearing at low pressures. These bands drop from much higher energy at -8 kB (not visible in Figure 2d), to immediately above the conduction band (Figure 2e). Although these bands play no role in determining the electronic properties of the framework, their rapid decrease in energy between -8 kB and -10 kB suggests that the energetics of the Ni-N interface is extremely sensitive to interatomic distance, and this interaction is antibonding in character. The bond lengths and associated energetics of this lattice contortion are presented in Figure 4 and more comprehensively in the Supplementary Information.

Contrastingly, monolayer  $\text{Ni}_3(\text{HIB})_2$  is persistently metallic upon both framework expansion and contraction. However, we noted that the converged structure of 10%-expanded

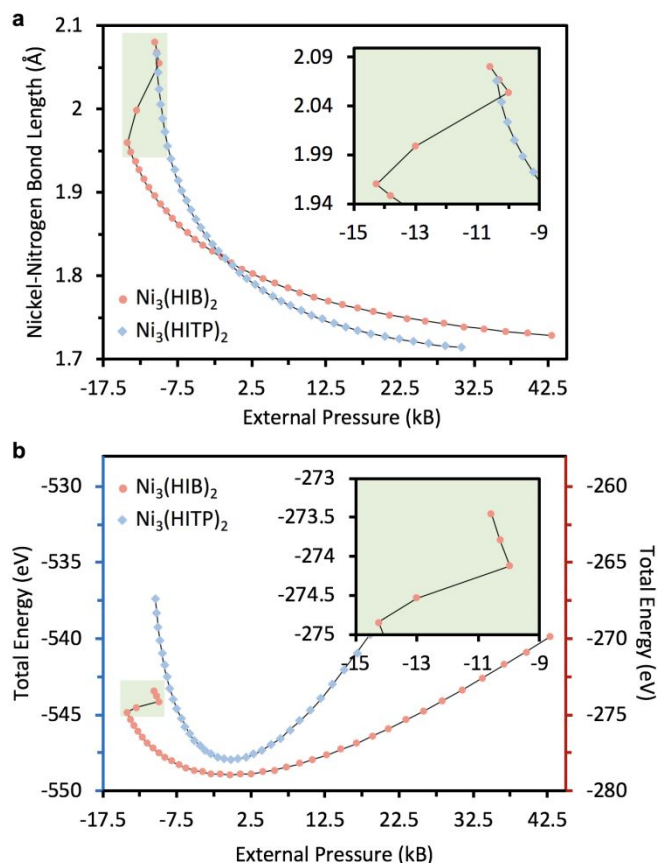


**Figure 4.** A structural (a) and energetic (b) comparison of both  $\text{Ni}_3(\text{HITP})_2$  and  $\text{Ni}_3(\text{HIB})_2$  at various pressures. The inset graphs highlight the  $\text{Ni}^{2+}$  piezoreduction upon expansion of the  $\text{Ni}_3(\text{HIB})_2$  lattice.

$\text{Ni}_3(\text{HIB})_2$  features a non-zero magnetic moment, corresponding to approximately 0.66 unpaired electrons per Ni. This electronic structure is at odds with any plausible electronic configuration for square planar  $\text{Ni}^{2+}$ .

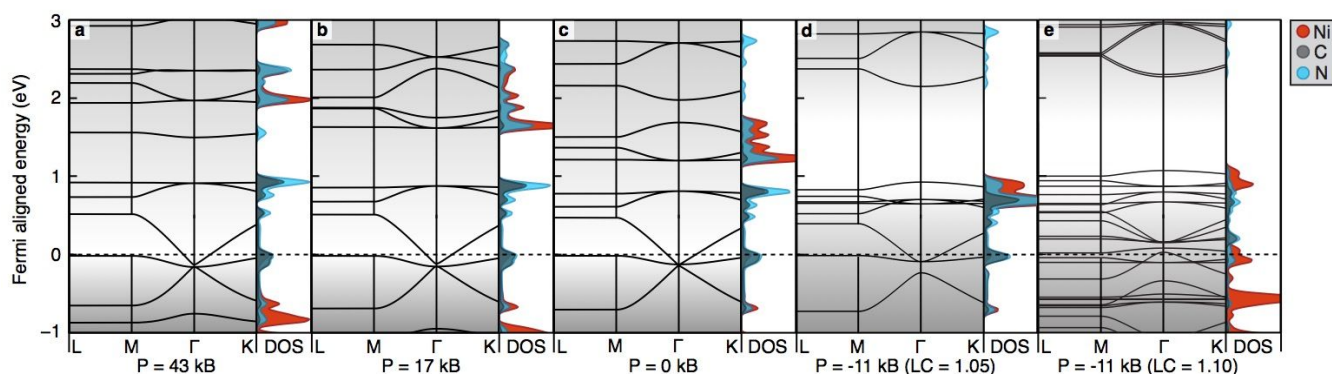


**Figure 3.** Electronic band structures and density of states plots for  $\text{Ni}_3(\text{HIB})_2$  under five representative hydrostatic pressures. LC = lattice constant. Ni-N antibonding bands drop below the Fermi level at -11 kB (LC = 1.10). The k-path from L-to-M (0.5,0,0.5-to-0.5,0,0) corresponds to the non-covalent direction and are flat because they are sampling perpendicular to the layer. M-to- $\Gamma$ -to-K sample in the intraplane covalent vectors (0.5,0,0-to-0,0,0-to-0.33,0.33,0).  $\text{Ni}_3(\text{HIB})_2$  is persistently a metal at all pressures, and the  $\text{Ni}^{2+}$  is piezoreduced at -11 kB (LC = 1.10).

We first assumed that the magnetic moment was due to an asymmetry in the expanded lattice resulting in an orbital degeneracy of  $d_{z^2}$  and  $d_{x^2-y^2}$ . However, examination of the converged material reveals that the structure is indeed symmetric. In fact,  $Ni^{2+}$  had been reduced by  $0.66 e^-$  per Ni, to  $Ni^{1.33+}$ . These two electrons are fully delocalised, in line with a Robin-Day type III classification. Bader analysis supported this observation with as evidenced by an increase in charge density on the nickel atoms<sup>43</sup>. We surmised that this reduction event was motivated by the electronic structure of the ligand, which may be thought of as a trianionic radical (one resonance form is shown in Figure 1d). While these electrons are paired and delocalized across the C-based  $\pi$ -system in the equilibrium structure, elongation of the Ni-N bond results in piezoreductive transfer of a ligand centred electron to the neighbouring Ni (Figure 4).

Beyond the electronic differences between the two structures, e.g. the piezoreductive transition observed in  $Ni_3(HIB)_2$ , and the semiconductor-to-metal transition in  $Ni_3(HITP)_2$ , the materials have different energetic responses to pressure. Figure 4a presents the explicit comparison of pressure to Ni-N bond length. Here, we observe three features; i) the equilibrium Ni-N bond length does not depend on the ligand, ii) as the lattice is contracted  $Ni_3(HITP)_2$  more rapidly contracts in the Ni-N bond than that observed for  $Ni_3(HIB)$  and, iii) as the lattice is expanded the piezoreductive transition occurs when the Ni-N bond length begins to exceed  $\sim 2 \text{ \AA}$ . The difference in Ni-N contraction can be attributed to the increased rigidity of the HITP ligand owing to an increase in dense covalent C-C bonds. Examination of total energy versus pressure (Figure 4b) reveals a similar trend;  $Ni_3(HIB)_2$  has a more shallow potential energy surface indicating that the HITP material is more rigid. This is further demonstrated through the structural comparison presented in the Supplementary Information.

Although we do not observe piezoreductive event in  $Ni_3(HITP)_2$  the Ni-N bands do drop in energy upon lattice expansion. In  $Ni_3(HIB)_2$  these bands drop below the Fermi level as external pressure decreases, and a formal reduction event occurs. Perhaps this transition is most obviously depicted by comparison of the Ni-N bond lengths, and corresponding energies (Figure 4). Energetically, this transition occurs with an input of 94 kcal/mol, and should be accessible in the laboratory setting.

## Conclusions

External pressure modulation of monolayer conductive MOFs such as  $Ni_3(HIB)_2$  and  $Ni_3(HITP)_2$ , leads to exotic electronic property transitions including band gap closing in semi-conductive monolayer of  $Ni_3(HITP)_2$ . The emergence of magnetic moments in the metallic monolayer is a result of the piezo-reductive transition of the metal centres.

As external pressure increases, slight changes in the electronic band structures occur for both monolayers. Interestingly,  $Ni_3(HITP)_2$  demonstrates a notable contraction in band gap energy as the lattice became progressively expanded, eventually becoming metallic at  $-10 \text{ kBar}$ . Additionally, lattice expansion showed that indeed the Ni-N

interface was the most labile and, in the case of  $Ni_3(HIB)_2$ , a piezoreduction occurs when the Ni-N bond length is expanded by approximately 10%.

Hydrostatic pressure therefore provides a pathway for electronic structure modifications in both semi-conducting and metallic materials. We expect these findings will aid in the development of novel MOF-based sensors, as well as serve as a general design consideration in the synthesis of other compressible, conductive MOFs.

## Computational Methods

Structural optimization of monolayer  $Ni_3(HIB)_2$  and  $Ni_3(HITP)_2$  were performed with DFT as implemented in the Vienna *ab initio* Simulation Package (VASP, version 5.4.4).<sup>44</sup> Both structures were equilibrated in a  $\sim 20 \text{ \AA}$  vacuum using the unrestricted GGA-PBEsol exchange-correlation functional.<sup>45</sup> Ionic relaxation was achieved when all forces were smaller than  $0.005 \text{ eV \AA}^{-1}$ . The plane-wave cut off was set at 500 eV and the SCF convergence criterion was  $10^{-6} \text{ eV}$ , resulting in electronic convergence of 0.005 eV per atom. An automatic k-grid was used during the optimization with  $4 \times 4 \times 1$  sampling, and yielded indistinguishable results compared to  $6 \times 6 \times 1$  meshes. Symmetry was not enforced.

From the equilibrated structures of  $Ni_3(HIB)_2$  and  $Ni_3(HITP)_2$  hydrostatic pressure was applied by scaling lattice constants in 0.5% increments. By allowing the stress tensor to be calculated at every electronic step while restricting the cell shape and cell volume to change, the external pressure was calculated at each lattice constant. Single point calculations were performed with a  $4 \times 4 \times 1$  which is a sufficient k-grid to model monolayer metallic  $Ni_3(HIB)_2$ . For  $Ni_3(HITP)_2$ , a higher k-grid of  $6 \times 6 \times 1$  were used to closely monitor the behaviour of the bands at the Fermi level and the flat bands corresponding to the Ni-N antibonding orbitals which are indistinguishable. These calculations were used to construct the electronic band structures and corresponding density of states for both MOFs at different pressures points. It should be noted that the DFT calculations employed here are known to systematically underestimate the band gap energy, especially for semiconductors<sup>46,47</sup>, so a larger band gap/dispersion perturbations may be possible in an experimental setting. The HSE06 hybrid functional was also examined and shows qualitatively similar properties to the PBEsol functional. This comparison is presented in the Supplementary Information.

Bader charge analysis was performed using the package by Henkelman and colleagues<sup>48</sup> (version 1.03) with core charge density correction was performed on optimized  $Ni_3(HIB)_2$  monolayer with lattice constant scaling of 100% and 110% to calculate the total charge differences of Ni atoms.

## Conflicts of interest

There are no conflicts to declare.

## Acknowledgement

This project was funded by the University of Oregon. All calculations were performed on the High-Performance

## Journal Name

Computing cluster at the University of Oregon (Talapas), and the Extreme Science and Engineering Discovery Environment (XSEDE) which is supported by National Science Foundation grant number ACI-1548562. Computations were also enabled by access to the PICS machine, Coeus, which is supported by the NSF (DMS1624776). We would also like to acknowledge Thomas W. Kasel and Jessica L. Fehrs for their valuable insights.

## References

- 1 A. K. Cheetham, C. N. R. Rao and R. K. Feller, Structural diversity and chemical trends in hybrid inorganic–organic framework materials, *Chem Commun*, 2006, 4780–4795.
- 2 H. K. Chae, J. Kim, Y. Go, M. Eddaoudi, A. J. Matzger, M. O’Keeffe and O. M. Yaghi, A route to high surface area, porosity and inclusion of large molecules in crystals, *Nature*, 2004, **427**, 523–527.
- 3 H. Furukawa, K. E. Cordova, M. O’Keeffe and O. M. Yaghi, The Chemistry and Applications of Metal–Organic Frameworks, *Science*, 2013, **341**, 1230444.
- 4 K. Xie, Q. Fu, C. Xu, H. Lu, Q. Zhao, R. Curtain, D. Gu, P. A. Webley and G. G. Qiao, Continuous assembly of a polymer on a metal–organic framework (CAP on MOF): a 30 nm thick polymeric gas separation membrane, *Energy Environ. Sci.*, 2018, **11**, 544–550.
- 5 M. Ding, R. W. Flaig, H.-L. Jiang and O. M. Yaghi, Carbon capture and conversion using metal–organic frameworks and MOF-based materials, *Chem. Soc. Rev.*, 2019, **48**, 2783–2828.
- 6 W. Liang, P. M. Bhatt, A. Shkurenko, K. Adil, G. Mouchaham, H. Aggarwal, A. Mallick, A. Jamal, Y. Belmabkhout and M. Eddaoudi, A Tailor-Made Interpenetrated MOF with Exceptional Carbon-Capture Performance from Flue Gas, *Chem*, 2019, **5**, 950–963.
- 7 O. K. Farha, A. Özgür Yazaydin, I. Eryazici, C. D. Malliakas, B. G. Hauser, M. G. Kanatzidis, S. T. Nguyen, R. Q. Snurr and J. T. Hupp, *De novo* synthesis of a metal–organic framework material featuring ultrahigh surface area and gas storage capacities, *Nat. Chem.*, 2010, **2**, 944–948.
- 8 E. D. Metzger, R. J. Comito, Z. Wu, G. Zhang, R. C. Dubey, W. Xu, J. T. Miller and M. Dincă, Highly Selective Heterogeneous Ethylene Dimerization with a Scalable and Chemically Robust MOF Catalyst, *ACS Sustain. Chem. Eng.*, 2019, **7**, 6654–6661.
- 9 P. Horcajada, C. Serre, M. Vallet-Regí, M. Sebban, F. Taulelle and G. Férey, Metal-organic frameworks as efficient materials for drug delivery, *Angew. Chem. Int. Ed Engl.*, 2006, **45**, 5974–5978.
- 10 J. An, S. J. Geib and N. L. Rosi, Cation-Triggered Drug Release from a Porous Zinc–Adeninate Metal–Organic Framework, *J. Am. Chem. Soc.*, 2009, **131**, 8376–8377.
- 11 C. Y. Lee, O. K. Farha, B. J. Hong, A. A. Sarjeant, S. T. Nguyen and J. T. Hupp, Light-Harvesting Metal–Organic Frameworks (MOFs): Efficient Strut-to-Strut Energy Transfer in Bodipy and Porphyrin-Based MOFs, *J. Am. Chem. Soc.*, 2011, **133**, 15858–15861.
- 12 C.-C. Lin, Y.-C. Huang, M. Usman, W.-H. Chao, W.-K. Lin, T.-T. Luo, W.-T. Whang, C.-H. Chen and K.-L. Lu, Zr-MOF/Polyaniline Composite Films with Exceptional Seebeck Coefficient for Thermoelectric Material Applications, *ACS Appl. Mater. Interfaces*, 2019, **11**, 3400–3406.
- 13 A. Vlad and A. Balducci, Supercapacitors: Porous materials get energized, *Nat. Mater.*, 2017, **16**, 161–162.
- 14 D. Sheberla, J. C. Bachman, J. S. Elias, C.-J. Sun, Y. Shao-Horn and M. Dincă, Conductive MOF electrodes for stable supercapacitors with high areal capacitance, *Nat. Mater.*, 2017, **16**, 220–224.
- 15 X. Zhang, P. Dong and M.-K. Song, Metal–Organic Frameworks for High-Energy Lithium Batteries with Enhanced Safety: Recent Progress and Future Perspectives, *Batter. Supercaps*, 2019, **2**, 591–626.
- 16 E. D. Spoerke, L. J. Small, M. E. Foster, J. Wheeler, A. M. Ullman, V. Stavila, M. Rodriguez and M. D. Allendorf, MOF-Sensitized Solar Cells Enabled by a Pillared Porphyrin Framework, *J. Phys. Chem. C*, 2017, **121**, 4816–4824.
- 17 H. Zhang, X. Liu, Y. Wu, C. Guan, A. K. Cheetham and J. Wang, MOF-derived nanohybrids for electrocatalysis and energy storage: current status and perspectives, *Chem. Commun.*, 2018, **54**, 5268–5288.
- 18 X. Fang, B. Zong and S. Mao, Metal–Organic Framework-Based Sensors for Environmental Contaminant Sensing, *Nano-Micro Lett.*, 2018, **10**, 64.
- 19 A. Walsh, K. T. Butler and C. H. Hendon, Chemical principles for electroactive metal–organic frameworks, *MRS Bull.*, 2016, **41**, 870–876.
- 20 C. H. Hendon, A. Walsh and M. Dincă, Frontier Orbital Engineering of Metal–Organic Frameworks with Extended Inorganic Connectivity: Porous Alkaline-Earth Oxides, *Inorg. Chem.*, 2016, **55**, 7265–7269.
- 21 N. N. K. Maity and S. Saha, in *Elaboration and Applications of Metal-organic Frameworks*, 2018, pp. 655–686.
- 22 S. Lin, P. M. Usov and A. J. Morris, The role of redox hopping in metal–organic framework electrocatalysis, *Chem. Commun.*, 2018, **54**, 6965–6974.
- 23 S. R. Ahrenholtz, C. C. Epley and A. J. Morris, Solvothermal Preparation of an Electrocatalytic Metalloporphyrin MOF Thin Film and its Redox Hopping Charge-Transfer Mechanism, *J. Am. Chem. Soc.*, 2014, **136**, 2464–2472.
- 24 L. S. Xie, L. Sun, R. Wan, S. S. Park, J. A. DeGayner, C. H. Hendon and M. Dincă, Tunable Mixed-Valence Doping toward Record Electrical Conductivity in a Three-Dimensional Metal–Organic Framework, *J. Am. Chem. Soc.*, 2018, **140**, 7411–7414.
- 25 J. G. Park, M. L. Aubrey, J. Oktawiec, K. Chakarawet, L. E. Darago, F. Grandjean, G. J. Long and J. R. Long, Charge Delocalization and Bulk Electronic Conductivity in the Mixed-Valence Metal–Organic Framework Fe(1,2,3-triazolate)<sub>2</sub>(BF<sub>4</sub>)<sub>x</sub>, *J. Am. Chem. Soc.*, 2018, **140**, 8526–8534.
- 26 L. Sun, C. H. Hendon, S. S. Park, Y. Tulchinsky, R. Wan, F. Wang, A. Walsh and M. Dincă, Is iron unique in promoting electrical conductivity in MOFs?, *Chem. Sci.*, 2017, **8**, 4450–4457.
- 27 D. Sheberla, L. Sun, M. A. Blood-Forsythe, S. Er, C. R. Wade, C. K. Brozek, A. Aspuru-Guzik and M. Dincă, High Electrical Conductivity in Ni<sub>3</sub>(2,3,6,7,10,11-hexamino-triphenylene)<sub>2</sub>, a Semiconducting Metal–Organic Graphene Analogue, *J. Am. Chem. Soc.*, 2014, **136**, 8859–8862.
- 28 L. Sun, B. Liao, D. Sheberla, D. Kraemer, J. Zhou, E. A. Stach, D. Zakharov, V. Stavila, A. A. Talin, Y. Ge, M. D. Allendorf, G. Chen, F. Léonard and M. Dincă, A Microporous and Naturally Nanostructured Thermoelectric Metal–Organic Framework with Ultralow Thermal Conductivity, *Joule*, 2017, **1**, 168–177.
- 29 J.-H. Dou, L. Sun, Y. Ge, W. Li, C. H. Hendon, J. Li, S. Gul, J. Yano, E. A. Stach and M. Dincă, Signature of Metallic Behavior in the Metal–Organic Frameworks M<sub>3</sub>(hexaiminobenzene)<sub>2</sub>(M = Ni, Cu), *J. Am. Chem. Soc.*, 2017, **139**, 13608–13611.
- 30 M. E. Foster, K. Sohlberg, C. D. Spataru and M. D. Allendorf, Proposed Modification of the Graphene Analogue Ni<sub>3</sub>(HITP)<sub>2</sub> To



- Yield a Semiconducting Material, *J. Phys. Chem. C*, 2016, **120**, 15001–15008.
- 31 M. E. Foster, K. Sohlberg, M. D. Allendorf and A. A. Talin, Unraveling the Semiconducting/Metallic Discrepancy in  $\text{Ni}_3(\text{HITP})_2$ , *J. Phys. Chem. Lett.*, 2018, **9**, 481–486.
- 32 Y.-X. Shi, W.-X. Li, W.-H. Zhang and J.-P. Lang, Guest-Induced Switchable Breathing Behavior in a Flexible Metal–Organic Framework with Pronounced Negative Gas Pressure, *Inorg. Chem.*, 2018, **57**, 8627–8633.
- 33 S. Krause, V. Bon, I. Senkowska, D. M. Töbrens, D. Wallacher, R. S. Pillai, G. Maurin and S. Kaskel, The effect of crystallite size on pressure amplification in switchable porous solids, *Nat. Commun.*, 2018, **9**, 1573.
- 34 K. Jiang, L. Zhang, Q. Hu, D. Zhao, T. Xia, W. Lin, Y. Yang, Y. Cui, Y. Yang and G. Qian, Pressure controlled drug release in a Zr-cluster-based MOF, *J. Mater. Chem. B*, 2016, **4**, 6398–6401.
- 35 S. A. Moggach, T. D. Bennett and A. K. Cheetham, The Effect of Pressure on ZIF-8: Increasing Pore Size with Pressure and the Formation of a High-Pressure Phase at 1.47 GPa, *Angew. Chem. Int. Ed.*, 2009, **121**, 7221–7223.
- 36 Y. H. Hu and L. Zhang, Amorphization of metal-organic framework MOF-5 at unusually low applied pressure, *Phys. Rev. B*, 2010, **81**, 174103.
- 37 A. U. Ortiz, A. Boutin, A. H. Fuchs and F.-X. Coudert, Metal-organic frameworks with wine-rack motif: what determines their flexibility and elastic properties?, *J. Chem. Phys.*, 2013, **138**, 174703.
- 38 J. Young Jung, F. Karadas, S. Zulfiqar, E. Deniz, S. Aparicio, M. Atilhan, C. T. Yavuz and S. Min Han, Limitations and high pressure behavior of MOF-5 for CO<sub>2</sub> capture, *Phys. Chem. Chem. Phys.*, 2013, **15**, 14319–14327.
- 39 A. J. Graham, D. R. Allan, A. Muszkiewicz, C. A. Morrison and S. A. Moggach, The Effect of High Pressure on MOF-5: Guest-Induced Modification of Pore Size and Content at High Pressure, *Angew. Chem. Int. Ed.*, 2011, **50**, 11138–11141.
- 40 C. Zhou, L. Longley, A. Krajnc, G. J. Smales, A. Qiao, I. Erucar, C. M. Doherty, A. W. Thornton, A. J. Hill, C. W. Ashling, O. T. Qazvini, S. J. Lee, P. A. Chater, N. J. Terrill, A. J. Smith, Y. Yue, G. Mali, D. A. Keen, S. G. Telfer and T. D. Bennett, Metal-organic framework glasses with permanent accessible porosity, *Nat. Commun.*, 2018, **9**, 5042.
- 41 C. H. Hendon, K. E. Wittering, T.-H. Chen, W. Kaveevivitchai, I. Popov, K. T. Butler, C. C. Wilson, D. L. Cruickshank, O. Š. Miljanić and A. Walsh, Absorbate-Induced Piezochromism in a Porous Molecular Crystal, *Nano Lett.*, 2015, **15**, 2149–2154.
- 42 R. Hoffmann, How Chemistry and Physics Meet in the Solid State, *Angew. Chem. Int. Ed. Engl.*, 1987, **26**, 846–878.
- 43 M. Xu, P. Xiao, S. Stauffer, J. Song, G. Henkelman and J. B. Goodenough, Theoretical and Experimental Study of Vanadium-Based Fluorophosphate Cathodes for Rechargeable Batteries, *Chem. Mater.*, 2014, **26**, 3089–3097.
- 44 G. Kresse and J. Furthmüller, Efficient iterative schemes for ab initio total-energy calculations using a plane-wave basis set, *Phys. Rev. B*, 1996, **54**, 11169–11186.
- 45 J. P. Perdew, A. Ruzsinszky, G. I. Csonka, O. A. Vydrov, G. E. Scuseria, L. A. Constantin, X. Zhou and K. Burke, Restoring the Density-Gradient Expansion for Exchange in Solids and Surfaces, *Phys. Rev. Lett.*, 2008, **100**, 136406.
- 46 A. Kumar, K. Banerjee, A. S. Foster and P. Liljeroth, Two-Dimensional Band Structure in Honeycomb Metal–Organic Frameworks, *Nano Lett.*, 2018, **18**, 5596–5602.
- 47 J. P. Perdew, K. Burke and M. Ernzerhof, Generalized Gradient Approximation Made Simple, *Phys. Rev. Lett.*, 1996, **77**, 3865–3868.
- 48 W. Tang, E. Sanville and G. Henkelman, A grid-based Bader analysis algorithm without lattice bias, *J. Phys. Condens. Matter*, 2009, **21**, 084204.